Supporting Information

Competitive Adsorption-Driven CO_2/N_2 Separation in Monolayer Fullerene Membranes with funnel-shaped pores

Ruirui Han[a], Jing Guan[a], Hongwang Lu[a], Yanping Ma,[b] Mingwen Zhao[a], Weifeng Li[a,], Yuanyuan Qu[a,]**

[a]School of Physics, Shandong University, Jinan 250100, China

[b]Dongying Science and Technology Innovation Service Center, Dongying 257091, China

* Correspondence authors. Email: quyuanyuan@sdu.edu.cn, lwf@sdu.edu.cn

Supplementary Figures

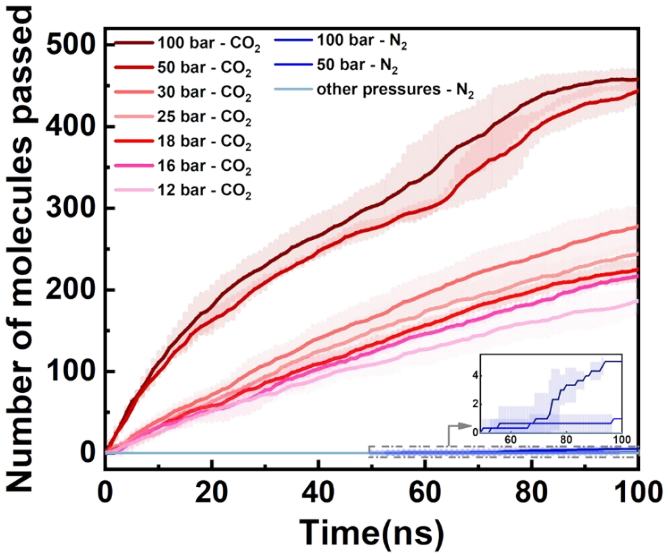

Fig. S1 Cumulative number of CO_2 and N_2 molecules permeating through the monolayer fullerene membrane as a function of simulation time under different pressures. Solid lines show the mean values averaged over independent runs, and the shaded bands represent the corresponding standard deviations. The inset depicts the number of passed molecules over the specified time interval.

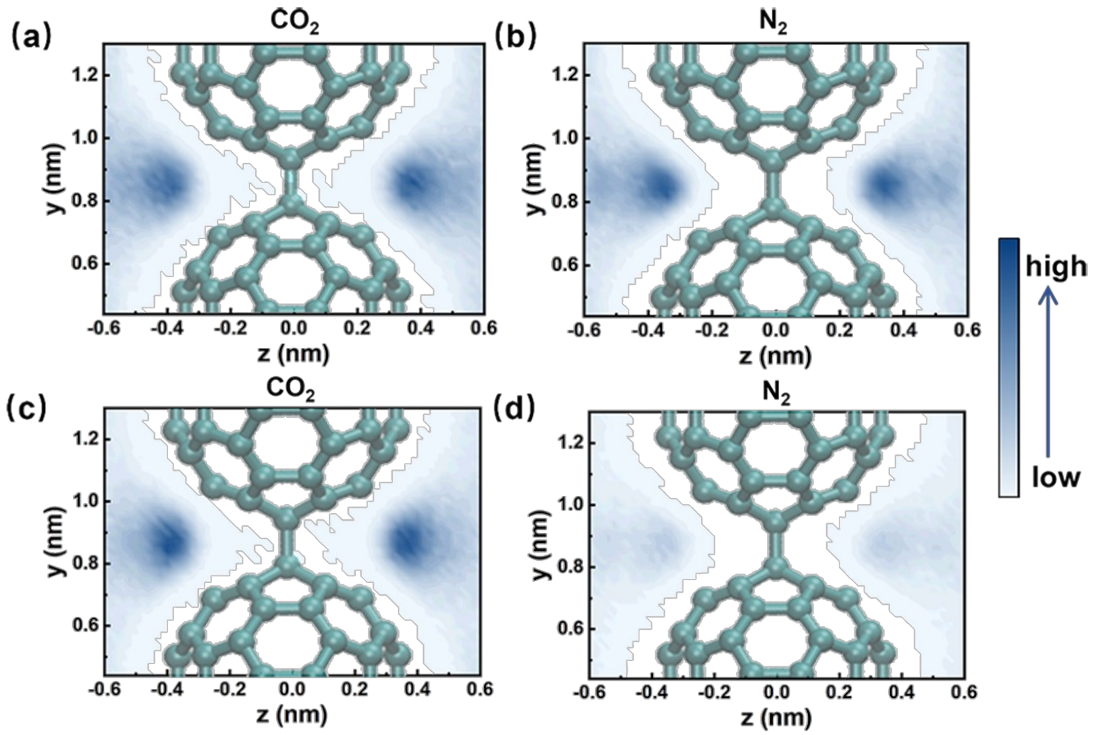

Fig. S2 In-plane probability density distributions for pure-gas system (a) and mixed-gas system (b) at 400 K. The monolayer fullerene membrane is located at z = 0.

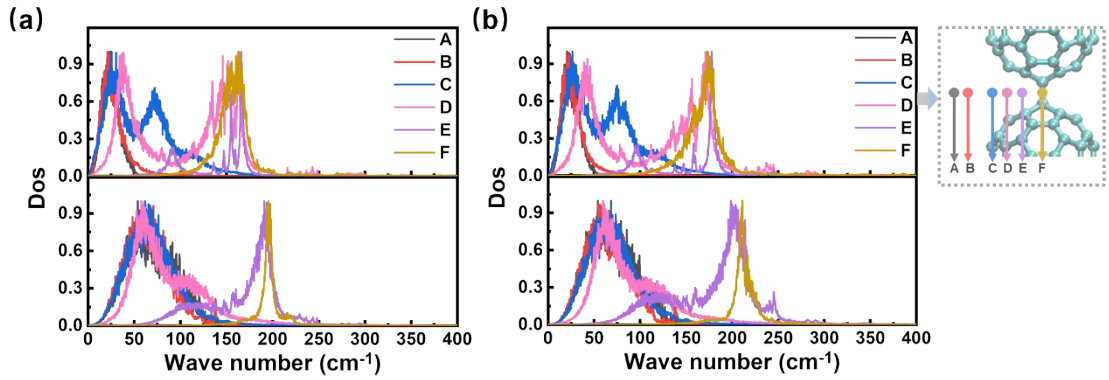

Fig. S3 (a) The RDOS analysis along the x-direction for CO_2 and N_2 under various positions. (b) The RDOS analysis along the y-direction for CO_2 and N_2 under various positions.

Supplementary Tables

Table S1. Force field parameters for membrane.

monolayer fullerene membrane			
	$\varepsilon\ (kJ\ /mol)$	$\sigma\ (nm)$	$q(e)$
C	0.355	0.2929	0
graphene			
	$\varepsilon(kJ\ /mol)$	$\sigma\ (nm)$	$q(e)$
CA	0.355	0.2929	0

Table S2. Force field parameters for CO_2 and N_2.

CO_2			
	$\varepsilon\ (kJ\ /mol)$	$\sigma\ (nm)$	$q(e)$
C	0.23388	0.2757	0.6512
O	0.66937	0.3033	-0.3256
bonds	length(Å)		
C-O	1.149		
N_2			
	$\varepsilon\ (kJ\ /mol)$	$\sigma\ (nm)$	$q(e)$
N	0.30265	0.3318	-0.4048
Center of Mass	0	0	0.8096
bonds	length(Å)		
N-N	1.098		

Table S3. Adsorption states and transition states of CO_2 and N_2 passing through the monolayer fullerene membrane.

	Adsorption State		**Transition State**	
	Top view	Side view	Top view	Side view
CO_2	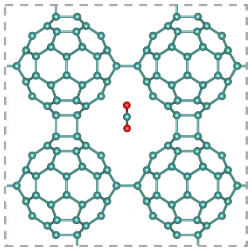	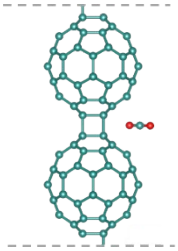	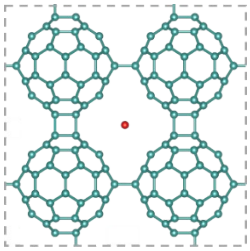	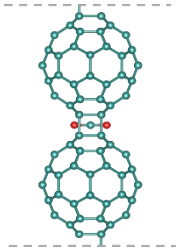
N_2	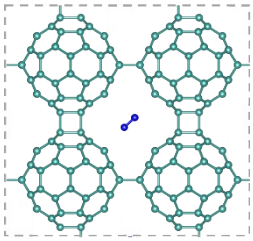	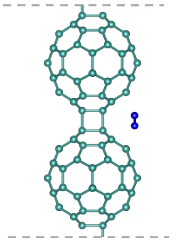	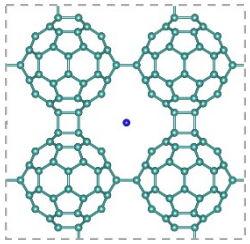	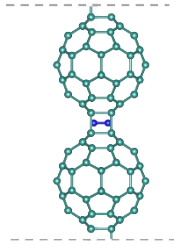

Table S4. Adsorption energies of CO_2 (E_{CO_2}) and N_2 (E_{N_2}) obtained from DFT and from MD calculations using OPLS-AA and AMBER99SB force fields.

Forcefield	E_{CO_2} (kJ/mol)	E_{N_2} (kJ/mol)
DFT	-24.12	-19.39
MD (OPLS-AA)	-10.26	-6.25
MD (AMBER99SB)	-10.08	-6.19

Supplementary Method

S1. Estimation of boundary layer mass transfer resistance and apparent selectivity

To estimate the influence of boundary-layer effect, we model the feed-side flow as internal laminar flow in a narrow rectangular channel representative of industrial gas separation modules. The characteristic length for mass transfer is taken as the hydraulic diameter D_h, and the following operating and physical properties are used:

Gas temperature: T = 300 K

Gas velocity: u = 2 m/s

Density: ρ = 1.18 kg/m^3

Viscosity: μ = 1.85 × 10^{-5} Pa · s

Binary diffusivity: D = 1.6 × 10^{-5} m^2/s

Hydraulic diameter: D_h = 1.0 × 10^{-3} m

The Reynolds and Schmidt numbers are[1]

$$Re = \frac{\rho u D_h}{\mu} = 127,\ Sc = \frac{\mu}{\rho D} \approx 0.98$$

For entrance-controlled laminar internal flow, the Sherwood number is approximately using a flat-plate-type correlation[2],

$$Sh = 0.664 Re^{1/2} Sc^{1/3} = 7.4$$

The corresponding gas-side mass transfer coefficient is

$$k_g = \frac{ShD}{D_h} \approx \frac{7.4 \times 1.6 \times 10^{-5}}{10^{-3}} \approx 0.12\ (m/s)$$

To express this resistance in the same units as the membrane permeance, we define an effective gas-side permeance

$$k_p = \frac{k_g}{RT}\ ,$$

where $R = 8.314\ J/mol/K$ and $T = 300\ K$, giving

$$k_p \approx \frac{0.12}{8.314 \times 300} \approx 4.8 \times 10^{-5}\ (mol/m^2/s/Pa)$$

The intrinsic permeances of the membrane are

$$P_{m,CO_2} = 2.11 \times 10^{-5}\ mol/m^2/s/Pa\ ,$$

$$P_{m,N_2} = 5.92 \times 10^{-9}\ mol/m^2/s/Pa\ ,$$

corresponding to an intrinsic selectivity $S = \frac{P_{m,CO_2}}{P_{m,N_2}} = 3564$.

The overall permeance including gas-side resistance is computed from resistances in series:

$$P_{tot,i} = \left(\frac{1}{k_p} + \frac{1}{P_{m,i}}\right)^{-1}$$

For CO_2,

$$P_{tot,i} \approx \left(\frac{1}{4.8 \times 10^{-5}} + \frac{1}{2.11 \times 10^{-5}}\right)^{-1} \approx 1.5 \times 10^{-5}\,(mol/m^2/s/Pa)\,,$$

giving

$$\frac{P_{tot,CO_2}}{P_{m,CO_2}} \approx 0.71\,.$$

Thus, boundary layer resistance reduces the effective CO_2 driving force by about 29%.

For N_2, because $P_{m,N_2} \ll k_p$, the boundary layer resistance is negligible and $P_{tot,N_2} \approx P_{m,N_2}$.

The apparent CO_2/ N_2 selectivity is then

$$S_{app} = \frac{P_{tot,CO_2}}{P_{tot,N_2}} = \frac{1.5 \times 10^{-5}}{5.92 \times 10^{-9}} = 2533$$

Therefore, for realistic channel dimension and flow conditions, the apparent CO_2/ N_2 selectivity remains higher than 2000 in the present of boundary-layer resistance.

S2. Knudsen defect model and tolerance analysis

To assess the tolerance of the monolayer fullerene membrane to nanoscale defects (pinhole pores), a simplified parallel-transport model was employed, in which the ideal selective region and the defect region are treated as two parallel pathways. The total membrane area is A; the defect-free region has area $(1-\phi)$A, and the pinhole region has area ϕA, where ϕ is the defect area fraction (defect porosity).

For component i (CO_2 or N_2), the overall area-averaged permeance $P_{i,eff}$ is written as an area-weighted sum of the contributions from the ideal and defect regions: [3]

$$P_{i,eff} = (1-\phi)P_{i,ideal} + \phi P_{i,leak}$$

where $P_{i,ideal}$ is the permeance of the ideal defect-free membrane, and $P_{i,leak}$ is the permeance through the pinhole leakage pathway. At 300 K, our MD results indicates permeance values of $P_{CO_2,ideal} =$ 2.11×10^{-5} mol m^{-2} s^{-1} Pa^{-1}, $P_{CO_2,ideal} =$ 5.92×10^{-9} mol m^{-2} s^{-1} Pa^{-1}.

The defect region is modeled as a collection of pinholes with an effective diameter of about 1nm (~1 fullerene defects) or 2 nm (~ 4 fullerenes defects), for which gas transport is approximated by Knudsen flow. In the Knudsen regime, the selectivity of component CO_2 over N_2 is

$$\alpha_{CO_2/N_2}^{Kn} = \sqrt{\frac{M_{N_2}}{M_{CO_2}}} \approx 0.8$$

In the Knudsen limit, the permeance through a cylindrical pore scale approximately linearly with the pore diameter *d* at fixed porosity and thickness. Therefore, we consider two representative defect sizes:

1. 2 nm pinholes (~ 4 fullerenes defects): A conservative CO_2 permeance of

$P_{CO_2,leak}^{(2nm)} =$ 10^{-4} mol m^{-2} s^{-1} Pa^{-1} is adopted to represent a highly permeable, weakly selective leakage pathway in the Knudsen or near-Knudsen regime.

2. 1 nm pinholes (~1 fullerene defects): For 1 nm defects, the characteristic diameter is halved. Assuming Knudsen-controlled transport, the permeance is scaled proportionally with *d*, leading to $P_{CO_2,leak}^{(1nm)} =$ 5×10^{-5} mol m^{-2} s^{-1} Pa^{-1}.

While the Knudsen selectivity α_{CO_2/N_2}^{Kn} remains unchanged because it depends only on the molar masses. The corresponding N_2 remains unchanged because it depends only on the molar masses. The corresponding N_2 permeances follow from

$$P_{N_2,leak}^{(d)} = \frac{P_{CO_2,leak}^{(d)}}{\alpha_{CO_2/N_2}^{Kn}}$$

For a given defect area fraction ϕ, the effective permeances of CO_2 and N_2 are

$$P_{CO_2,eff}^{(d)} = (1-\phi)P_{CO_2,ideal} + \phi P_{CO_2,leak}^{(d)}$$

$$P_{N_2,eff}^{(d)} = (1-\phi)P_{N_2,ideal} + \phi P_{N_2,leak}^{(d)}$$

The corresponding overall CO_2/N_2 selectivity is

$$\alpha_{CO_2/N_2,\ eff}^{(d)} = \frac{P_{CO_2,eff}^{(d)}}{P_{N_2,eff}^{(d)}}$$

By scanning ϕ from 0 up to a chosen upper limit and evaluating $\alpha_{CO_2/N_2,\ eff}^{(d)}$, a tolerance map is obtained at that relates defect porosity to overall selectivity.

References

(1) Li X.; Younas M.; Rezakazemi M.; Ly Q.V.; Li J. A review on hollow fiber membrane module towards high separation efficiency: Process modeling in fouling perspective [J]. *Chin. Chem. Lett*, **2022**, 33(8): 3594-3602.

(2) Abdul Majid O.; Kuznetsova M.; Castel C.; Favre E.; Hreiz R. Impact of Concentration Polarization Phenomena on Gas Separation Processes with High-Performance Zeolite Membranes: Experiments vs. Simulations. *Membranes*. **2024**, 14(2):41.

(3) Bünger, L.; Kurtz, T.; Garbev, K.; Stemmermann, P.; Stapf, D. Mixed-Matrix Organo–Silica–Hydrotalcite Membrane for CO_2 Separation Part 2: Permeation and Selectivity Study. *Membranes,* **2024**, 14, 156.